AIP | Review of Scientific Instruments

1D fast coded aperture camera

Magnus Haw and Paul Bellan

Citation: Review of Scientific Instruments **86**, 043506 (2015); doi: 10.1063/1.4917345
View online: http://dx.doi.org/10.1063/1.4917345
View Table of Contents: http://scitation.aip.org/content/aip/journal/rsi/86/4?ver=pdfcov
Published by the AIP Publishing

1D fast coded aperture camera

Magnus Haw[a] and Paul Bellan
Department of Applied Physics and Materials Science, Caltech, 1200 E. California Blvd. MC 128-95, Pasadena, California 91125, USA

(Received 23 February 2015; accepted 31 March 2015; published online 29 April 2015)

A fast (100 MHz) 1D coded aperture visible light camera has been developed as a prototype for imaging plasma experiments in the EUV/X-ray bands. The system uses printed patterns on transparency sheets as the masked aperture and an 80 channel photodiode array (9 V reverse bias) as the detector. In the low signal limit, the system has demonstrated 40-fold increase in throughput and a signal-to-noise gain of ≈7 over that of a pinhole camera of equivalent parameters. In its present iteration, the camera can only image visible light; however, the only modifications needed to make the system EUV/X-ray sensitive are to acquire appropriate EUV/X-ray photodiodes and to machine a metal masked aperture. © *2015 AIP Publishing LLC.* [http://dx.doi.org/10.1063/1.4917345]

I. INTRODUCTION

Measuring high energy radiation (>100 eV) is challenging because it cannot be focused by conventional lenses or mirrors. As a result, the most common imaging techniques for high energy radiation are pinhole and collimation. Unfortunately, both of these techniques rely on blocking the majority of incident radiation to form an image.

Coded or masked apertures are an alternative high energy imaging technique with much better signal to noise ratio (SNR) than pinhole or collimation imaging.[1] They were initially developed for X-ray astronomy in the 1970s[2,3,17,18,21] and have since been applied in medical imaging,[4] high energy particle imaging,[5] and chemical spectroscopy.[6] Despite the vast advantage in SNR offered by coded apertures, the technique has been slow to catch on, perhaps due to the lack of computational power when it was first suggested. However, all computational hurdles have long been surpassed and, for any diagnostic using a pinhole camera that suffers from low signal, this technique can be used to great effect.

Coded apertures consist of a 1 or 2 dimensional mask, composed of transparent and opaque elements, which is placed in front of a detector. Each transparent element acts like a pinhole camera, projecting an image on the detector. Given an appropriate pattern of these transparent elements, the detected superposition of pinhole images can be inverted to recover the original image. The advantage in signal scales like N, where N is the number of transparent elements.[4,7] If the dominant source of noise is shot noise (i.e., discretization noise where the number of detected counts is small), then the noise scales like $\sqrt{N}$ and the corresponding signal-to-noise ratio scales like $\sqrt{N}$ as well.

In this paper, Sec. II will cover theory, Sec. III will cover design and construction, Sec. IV will discuss simulation and perturbations, and Sec. V will cover results.

II. THEORY

Coded aperture imaging relies on projecting incident light through a mask pattern into an invertible superposition of shadow patterns on a detector. This results in a two step imaging process: projecting the source light through a mask pattern to encode the image and the decoding scheme for the detected image.

A. Image projection

For an arbitrary mask pattern, the detected image, D, will be the source intensity modulated by the mask transmission characteristics. In the far-field approximation (i.e., the intensity from a point source is approximately uniform across the detector[4,23]), the projected image can be represented as a convolution of the mask transmission, M, and the source intensity distribution, S,

$$D = S * M. \tag{1}$$

Due to issues with mask construction, most coded apertures are composed of discrete opaque or transparent elements (transmission of 0 or 1).[1,7]

For these discrete systems, the simplest scheme is for each resolved source to project a single mask element onto a single detector; this resolves any ambiguities produced by edge effects of partial illumination and greatly simplifies the convolution. With this constraint in mind, we can derive the spacings and field of view (FOV) for a given system.

To achieve 1-to-1 projection of mask elements onto detector elements, the placement of the mask (see Figure 1) is constrained by the ratio of detector element size, d, to mask element size, m,

$$\frac{d}{m} = \frac{a+b}{a} = \frac{z}{a}, \tag{2}$$

where z is the source-detector distance, a is the source-mask distance, and b is the mask-detector distance. In this case, the magnification of the mask pattern, $\frac{d}{m} \in [1, \infty]$, constrains the system spacing. The source-detector distance, z, is then

[a]Electronic mail: mhaw@caltech.edu

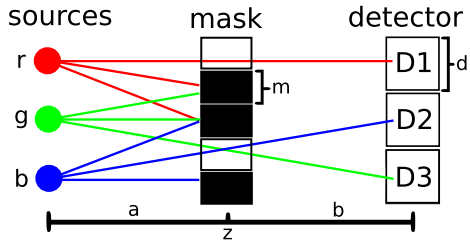

FIG. 1. Example of coded aperture with 3 detector elements. The source-mask distance is a, the mask-detector distance is b, and the total distance is z. The mask element length is m and the detector element length is d.

$$z = \frac{d}{m}a = \frac{b}{1-\frac{m}{d}}. \tag{3}$$

We can also solve for the FOV for a detector of n elements. By design, each source projects n mask elements onto the detector. This means we must have $2n-1$ individual mask elements: the first source requires n mask elements and the remaining $n-1$ sources each require an additional mask element (see Figure 1). Solving for the FOV,

$$FOV = nd + \frac{(2n-1)m - nd}{b}z = \frac{n-1}{\frac{1}{m}-\frac{1}{d}}, \tag{4}$$

we find that the FOV depends on the detector element size, mask element size, and the number of detector elements.

B. Inverting the image in 1D

Inverting the detected image first requires an invertible mask pattern. The condition that determines whether a mask is invertible is that each point source projects a unique, linearly independent pattern on the detector. In the case where the far-field approximation is valid, we can discretize the source distribution into n resolved pixels, where n is the number of detectors; in this approximation, the projection calculation becomes a matrix multiplication. Each subsequence of n mask elements projected onto the detector corresponds to a row of the projection matrix; if all rows are linearly independent, the projection of the mask is invertible.

Figure 1 demonstrates this for the case of three detectors: the top source projects the top 3 mask elements (1,0,0) giving the first row of the projection matrix. The other two sources project linearly independent subsequences of three (0,0,1), (0,1,0) giving an invertible transformation matrix, M,

$$D = M * S,$$
$$\begin{pmatrix} D_1 \\ D_2 \\ D_3 \end{pmatrix} = \begin{pmatrix} 1 & 0 & 0 \\ 0 & 0 & 1 \\ 0 & 1 & 0 \end{pmatrix} * \begin{pmatrix} r \\ g \\ b \end{pmatrix}.$$

To recover the initial image, one simply multiplies the detected array, D, by the inverse of the projection matrix.

C. Mask patterns

The next question is how to find invertible mask patterns of length $2n-1$. The simplest method is to guess and check with random sequences. The advantage of this method is that one can choose any open fraction of the mask (percentage of mask that is transparent); the disadvantage is that there is no guarantee of finding an invertible pattern.

However, there are also classes of invertible analytic sequences. The most popular of these classes are the cyclic difference sets.[22] There are many names and classifications for cyclic difference sets: Singer sets, pseudo-noise sequences, Paley sets, Hadamard sets, m-sequences, quadratic residues, twin prime sets, etc.; however, they all share the same property: each register shift of the sequence is linearly independent of every other. To make a 1D mask of length $(2n-1)$ from a cyclic difference sequence (CDS) of length (n), one concatenates two periods of the CDS with the last element of the second period omitted. This procedure was used in the mask shown in Figure 1: the CDS sequence in this case is (1,0,0) and the mask sequence is (1,0,0,1,0). This ensures that each resolved position projects a different register shift of the CDS on the detector, resulting in an invertible transform. Another useful property of these sequences is that the negative image of any CDS (i.e., exchanging 1's and 0's) is also a CDS.

There are a myriad of construction formulae for different cyclic difference sets which can be found in Refs. 4, 8, and 9. In this work, we present only a single construction method for sequences of length 2^k-1 that relies on the coefficients (mod 2) of primitive polynomials of degree k. This method is taken from Nelson and Fredman.[9]

We construct the fundamental sequence of length 2^k-1 by arbitrarily choosing the first k elements, $\{e_i\,; i = 1, \ldots, k\}$, and finding the remaining elements as follows:

$$e_{j+k} = \mathrm{mod}2\left(\sum_{i=0}^{k-1} a_i e_{j+i}\right), \tag{5}$$

where a_i is the coefficient of a primitive polynomial of degree k. An example for a 15-element sequence: we use one of the two primitive polynomials of degree 4, $P(x) = 1 + x + x^4$; $a_0 = 1, a_1 = 1, a_2 = 0, a_3 = 0$, and choose the first four elements to be 1. This gives the following sequence of length 15: [1,1,1,1,0,0,0,1,0,0,1,1,0,1,0].

D. Signal to noise ratio

Coded apertures were designed to minimize shot noise by more efficient use of the detector and thus improve the SNR by $\sim\sqrt{N}$. Accorsi[10] derives an expression for SNR on a pixel-by-pixel basis. This derivation assumes Poisson counting statistics and defines several parameters: fraction of counts from background ξ, finite transparency of opaque elements t, open mask fraction ρ, total number of pixels N_T, total intensity I_T, and the fraction of total intensity emitted by pixel ij, ψ_{ij},

$$SNR_{ij} = \frac{\sqrt{N_T I_T}\sqrt{\rho(1-\rho)}(1-t)\psi_{ij}}{\sqrt{(1-t)[\rho+(1-2\rho)\psi_{ij}]+t+\xi}}. \tag{6}$$

Using this expression, one can optimize the mask for SNR based on the parameters of one's setup. For the case of imaging a single point source with a perfect mask and no background ($\psi_{ij} = 1$, $\xi = 0$, $t = 0$), the expression reduces

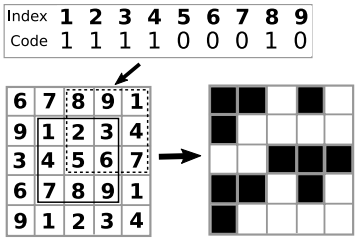

FIG. 2. This figure depicts folding a 2D sequence into a 2D invertible mask. Start with a 1D cyclic difference sequence (shown at top with associated indices). Next fold sequence such that every sub-square of 9 mask elements projects a register shift of the original sequence: solid sub-square has zero register shift and dotted sub-square has 2 element register shift. Finally, fill in sequence to obtain a 2D pattern.

to $\sqrt{\rho N_T I_T} = \sqrt{N I_T}$, where N is the number of transparent elements in the mask. Hence, we recover the basic $\sqrt{N}$ scaling for the case of a point source. For this case, the optimal mask, with respect to SNR, is the anti-pinhole mask with only one opaque element, $\rho = \frac{N_T - 1}{N_T}$. However, for more distributed sources, $\psi_{ij} \ll 1$, the optimal open fraction is reduced and the SNR gains are smaller. For these more distributed sources, it is useful to define some global figure of merit such as $FOM = \Sigma_{ij} \mathrm{SNR}_{ij}$.

For the Caltech jet experiment, background interference (e.g., electromagnetic interference, EMI) is large and in this large background limit ($\xi \gg 1$), Eq. (6) gives an optimal open fraction around 50%.

E. Moving to 2D

For most applications, with the notable exception of spectroscopy, it is desirable to have a 2D coded aperture. Conveniently, the only requirement is folding an invertible 1D sequence into 2D. The same principle applies for invertibility: each resolved source must project a linearly independent shadow pattern. Figure 2 demonstrates folding a 9-element cyclic difference sequence into a 2D mask: every sub-square of 9 mask elements projects a different register shift of the original sequence (Figure 3).

The projection matrix of the 2D mask is similar to that of the 1D mask: a 2D matrix with rows corresponding to the shadows cast by particular source positions. Each matrix row will correspond to the register shift of a CDS given by the projected sub-rectangle (Figure 2).

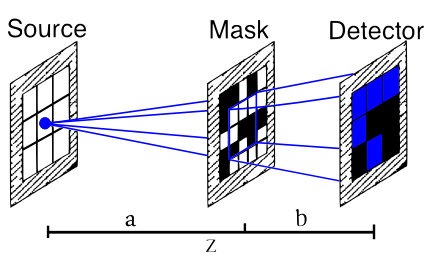

FIG. 3. Canonical representation of 2D coded aperture system: a light source, S, a coded aperture or mask, M, and the detector, D. A source at the center of the field of view projects the central sub-square of 9 mask elements onto the 9 detector elements.

III. DESIGN

The initial motivation for the project was to image EUV/X-ray bursts from fast (~1 μs) magnetic reconnection events in the Caltech plasma jet experiment.[11,12] Imaging these events requires very fast time resolution and high sensitivity. The visible light prototype was designed within these constraints with portability to an EUV/X-ray system in mind.

A. Detector

Due to the constraints of the EUV bursts, namely, 1-2 μs events occurring over a 30 μs plasma lifetime, the system must be sensitive on a μs timescale. To satisfy this timescale, a photodiode array was chosen as the detector. Photodiodes of small size under reverse bias have much faster response time as compared with CMOS and CCD detectors. Reverse biasing the photodiode arrays greatly increases their dynamic range and prevents saturation at high light intensity. Five 16-element photodiode arrays (A2V-16)[13] from OSI Optoelectronics, Inc., were chosen as the detectors because their mechanical design allows for continuous linear mounting. The arrays are mounted in sockets on a printed circuit board and placed inside a shielded box with a slit aperture. BNC cables connect each channel to the digitizer and all five arrays are reversed biased by four 9 V batteries in parallel; no amplifiers were needed.

The digitizer is a 96-channel (e.g., twelve 8-channel 3300 Versa Module Europa panels) system from Struck Innovative Systems. Each channel has a sampling rate of 100 MHz, 12-bit dynamic range, 50 Ω input impedance, 32 kB memory, and an input range of −512 to 512 mV with continuously adjustable offset. Circuit diagram shown in Figure 4.

B. Mask

The mask was made by printing out appropriate patterns on standard transparency paper (Fig. 5). This made fabrication accessible, inexpensive, and fast, which was essential in testing different mask patterns. New mask patterns could be generated, printed on the office printer, and tested on

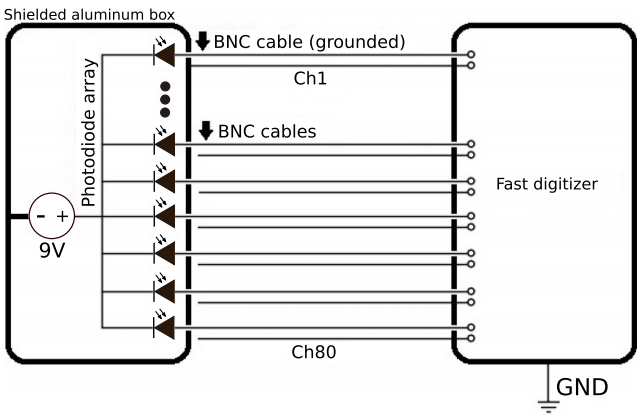

FIG. 4. Circuit diagram of coded aperture detector system. Shielded box for photodiode array is grounded through a single BNC cable to eliminate ground loops.

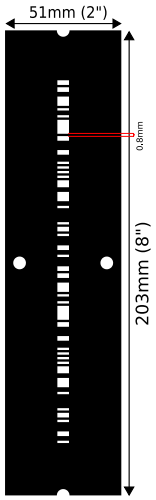

FIG. 5. Image showing mask dimensions for mask with element size 0.8 mm (1/32″). Additional circular holes are for mounting and alignment purposes.

the experiment within 15 minutes. Two copies of a printed pattern were stacked together to increase the optical density of the opaque elements. Mask element dimensions ranged from $m = 1.5875$ mm (1/16″) to $m = 0.79375$ mm (1/32″). Mask patterns were translated into JPEG images using a Python script and printed to scale by setting the pixels per inch (PPI) resolution.

C. Mounting

The mounting for the system is important as the system relies on geometric optics: placement of the mask and detector determines the focal length and FOV [Eqs. (3) and (4)]. The photodiode array was mounted inside a shielded box with a slit aperture. The mask was mounted on adjustable rails attached to the main stand (Fig. 6). This allowed the focal length to be adjusted by sliding the rails while maintaining vertical alignment. For imaging through a given window on the vacuum chamber, the distance to the plasma was measured, the focal length was adjusted accordingly, and the FOV, relative to the chamber, was found by shining a laser array from the detector through the mask. To prevent light from outside the field of view from entering the detector, horizontal baffles were required along the length of the rails.

IV. SIMULATION AND PERTURBATIONS

In addition to the physical apparatus, a 3D coded aperture simulation was developed in Python to determine the severity of potential perturbations. The simulation inputs are the positions and orientations of light sources, mask elements, and detector elements. Single light sources are represented as point sources and distributed sources are formed by using a high density of point sources. Light projection from sources to detector is accomplished via ray tracing from each point source. Rays that pass through mask elements are deleted and the remaining rays passing through each detector element are counted. Rays were distributed uniformly spherically and it was found that convergence was achieved with >20 rays per source per detector. This ray formulation allows for testing of perturbations in 3D as well as accounting for the inverse square intensity of light sources.

Using this simple simulation, several perturbations to the system were examined: misalignment of mask, partially coded sources, and out of focus sources (depth sensitivity).

A. Mask alignment

Several different misalignments of the mask were tested using the simulation: vertical and horizontal offsets, tilt towards sources, and rotation around axis of sight. For these comparisons, the simulation test setup used a 15 element 1D detector array using a 29 element mask, imaging an off-center Gaussian peak, $\sigma = 6\%$ FOV. A smaller detector array was chosen for these benchmark tests to reduce simulation time.

For vertical (along the FOV dimension) perturbations, the FOV will shift by the number of mask elements displaced. Horizontal perturbations for the one-dimensional detectors only shift the field of view but in 2D will have the same issues as the vertical perturbations in 1D. It was found that tilting the mask towards or away from the detector

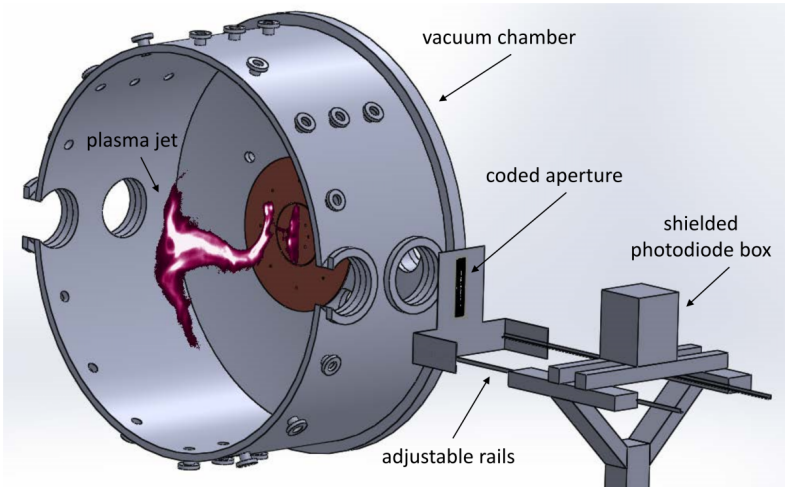

FIG. 6. Drawing depicting the coded aperture camera in relation to the plasma jet.

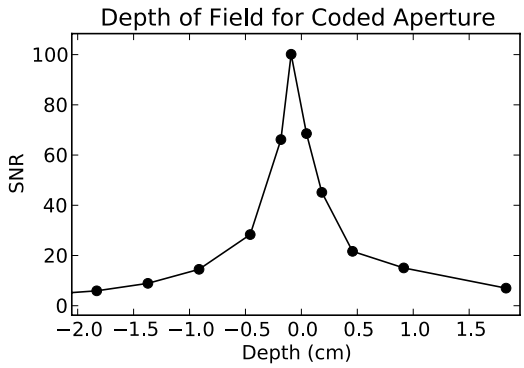

FIG. 7. Simulated depth of field for coded aperture system. The system can accurately reconstruct source distributions in a depth range of 1-2 cm. Outside of this range, sources will be out of focus and contribute noise.

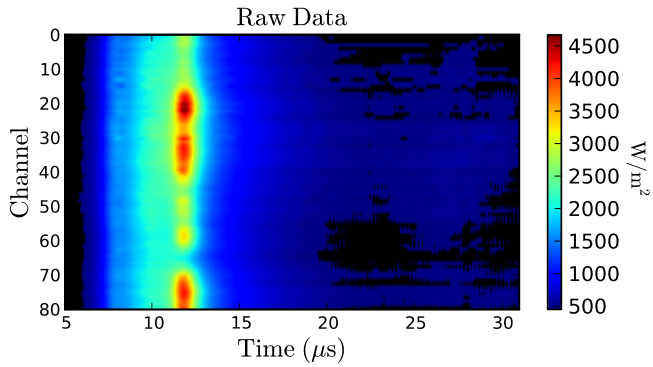

FIG. 9. Typical raw voltage data collected by the photodiode array.

has little effect for angles less than 10°. Rotations of the mask along the axis of sight were not significant until mask elements were rotated out of the source-detector plane (in general, $\omega_{max} < \sin^{-1}(h/(mn))/2$, where h is the horizontal width of a mask element). Consequently, for long thin arrays and 2D arrays, the rotational alignment must be fairly accurate.

B. Depth sensitivity

Since the coded aperture technique relies on proper projection of patterns, the sources must be at the correct distance for crisp images. To determine the depth sensitivity of the apparatus, the full 80 channel system was simulated using appropriate distances for a mask spacing, $m = 0.8$ mm and a detector element length, $d = 1.6$ mm. To estimate the depth of field, a single point source was used and the signal to noise ratio was calculated as the ratio of the single peak to the RMS of the remaining FOV. It was found that the system has a depth of field of 1-2 cm (Fig. 7).

Tomography using coded apertures has been of interest for some time.[4,14] However, this requires resolving small changes in the size of shadow projections, effectively requiring heavy oversampling. In general, one can expect the depth resolution to be at least 5 times worse than the spatial resolution.[4]

C. Partially coded field of view

The partially coded field of view is defined as those areas adjacent to the field of view which can still project light through the mask onto the detector (Fig. 8). This region extends a distance as large as the original field of view on all sides. Sources in this region will project an incomplete pattern on the detector that will be inverted as some arbitrary superposition of values (positive and/or negative) over the entire field of view. Since the resulting superposition is non-physical, the relative magnitude of the perturbation in a reconstructed image can be much larger than the relative signal intensity of the partially coded source. If strong negative intensities are visible in the inverted image, it may be an indication that partially coded sources are present. To prevent light from partially coded regions from reaching the detector, one must extend baffles from the detector to the source plane. Unfortunately, extending baffles to the source plane is impractical in many cases (e.g., astronomy) and, in these situations, the coded aperture cannot image subsections of bright objects.

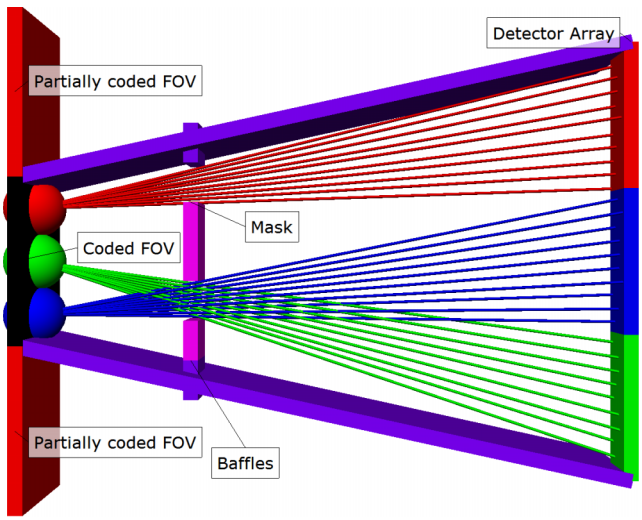

FIG. 8. The coded and partially coded fields of view are shown with respect to the mask-detector pair in Figure 1. Extended baffles are displayed, blocking light from partially coded regions.

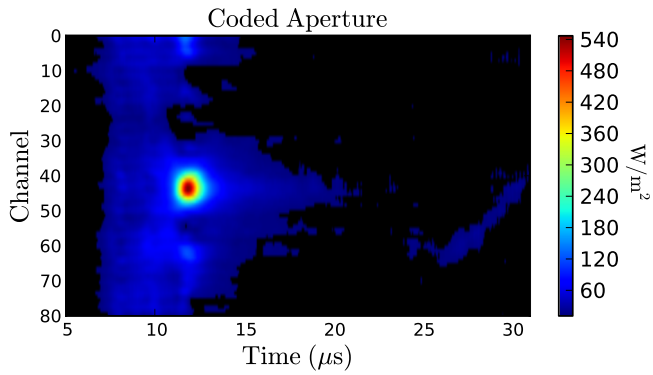

FIG. 10. Typical coded aperture image of plasma jet cross section obtained after decoding. Resolution is 2.8 mm/channel. Scale bar on the right ranges from 10 to 540 W/m^2.

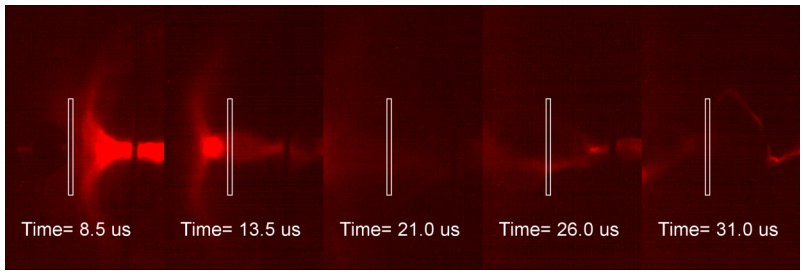

FIG. 11. Sequence of images of plasma jet taken with fast ICCD camera (Imacon 200). The FOV of the coded aperture camera is outlined in white.

V. RESULTS

The camera has been used to image a radial cross section of the Caltech plasma jet experiment.[11,12,15] We present here basic tests confirming that the coded aperture performs as expected.

A. Image reconstruction

Several data reduction steps were taken before image reconstruction. First, the initial data (Figure 9) were smoothed using a 200 ns Gaussian window to remove high frequency EMI (>15 MHz) from the raw signal. Second, the calibration of the photodiode array was applied (accounting for background levels and relative sensitivity of each element). Finally, any negative voltages (due to noise) still present in the raw data were set to zero. From these reduced raw data, the coded aperture inversion was applied, yielding physical images.

A typical reconstructed image is shown in Figure 10. 2D images of the plasma jet taken with an intensified charge-coupled device (ICCD) camera (Imacon 200) are shown in Figure 11 for comparison. The major features visible in the coded aperture image are the jet front and the kinking of the jet axis.[11,15,16,19,20] The relative intensities of the jet front and the jet axis differ by a factor of 20-50. The jet axis undergoes a kink instability where the axis accelerates into an expanding spiral. This spiral shape is projected in the coded aperture image as sinusoidal motion of the axis center.

Comparing each of these features with the 2D camera images, we find quantitative agreement in position, intensity ratios, and timing. The dynamic range of the coded aperture is greater than that of the ICCD, (ICCD pixels are 10-bit, coded-aperture pixels are 12-bit) and this aids in resolving the large range in plasma light intensity. Given this agreement, we are confident that the coded aperture reconstructions are valid images.

B. Comparison with pinhole camera

To benchmark the coded aperture images, they were compared with images taken using an equivalent pinhole mask on the same apparatus (i.e., a pinhole mask with same resolution and FOV as the coded aperture). For this instrument, the coded aperture mask gives an integrated raw signal roughly 40 times greater than that of the pinhole mask (Table I, Figs. 9 and 12). This meets the expectation for a 50% open mask: a given source will illuminate approximately half of the detectors giving an $n/2$ increase in signal relative to a pinhole, where $n = 80$ is the number of detectors. The coded aperture camera can resolve features down to 10 W/m^2 whereas the pinhole camera can only resolve features down to 100 W/m^2. Even for an especially bright plasma shot, such as the one shown in Figure 12, the pinhole camera is unable to resolve the kinking of the jet axis.

If we define the signal to noise ratio as the intensity ratio of the brightest versus the dimmest identifiable feature, then the coded aperture image has about an order of magnitude better SNR as compared with the pinhole camera. This matches the expectation of square-root scaling of SNR.

TABLE I. Comparison of SNR for coded aperture and pinhole.

	Brightest feature (W/m^2)	Dimmest feature (W/m^2)	SNR
Coded aperture	540	10	54
Pinhole camera	760	100	7.6

C. Measurement of kink instability

Since the jet axis motion is visible in the coded aperture images, we can use this to estimate the acceleration present during the kink instability. To obtain an estimate of radial acceleration, we account for projection effects by inferring the angular position at the points where the kink crosses the initial axis position. From these points, we linearly interpolate the angular position from 16-30 μs. Then, the angular projection of a constant radial acceleration is fit to the image data. For

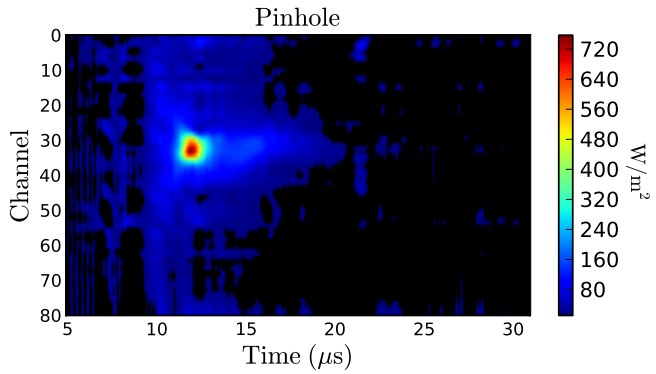

FIG. 12. Image of plasma jet taken with pinhole mask. This was an especially bright shot (≈40% brighter than average) chosen to illustrate the limited sensitivity of the pinhole configuration. The jet axis disappears at an intensity of 100 W/m^2. Scale bar ranges from 10 to 760 W/m^2. Resolution is 2.8 mm/channel.

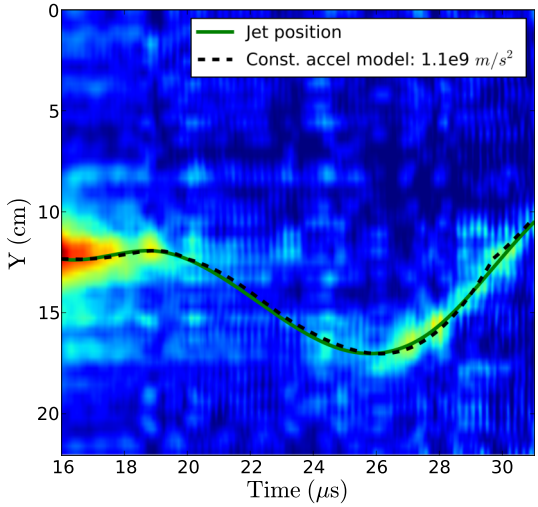

FIG. 13. Plot showing jet intensity over time, fit to jet axis as function of time, and a constant radial acceleration model. Fit to jet position is done by fitting a Gaussian profile at each time step and smoothing the resulting positions.

the plasma shot shown in Figure 13, the constant acceleration model of the radial motion fits quite well from 16-30 μs. Other plasma shots also exhibited constant accelerations in the range [6e8,1e10] m/s^2. This range of accelerations is consistent with previous measurements taken with the fast camera.[16]

VI. DISCUSSION

We have presented the design and first results of a fast (100 MHz) 1D coded aperture system for visible light. First tests show that the system properly reconstructs 1D cross sections and scales linearly with incident light intensity. Further measurements show that the system has ~7 times larger signal to noise ratio than an equivalent pinhole camera. A simulation was written to test various perturbations and it was found that the most significant perturbations were rotation of the mask around the axis of sight and light sources in the partially coded regions.

In addition to fulfilling its role as a prototype for an EUV/X-ray system, the system was able to provide high resolution measurement of the radial motion of the Caltech plasma jet as it goes kink-unstable.

The next step will be to move the system inside the vacuum chamber and replace the photodiodes with EUV/X-ray diodes. The system will then be used to study the distribution of EUV/X-ray bursts associated with magnetic reconnection.

ACKNOWLEDGMENTS

The authors would like to thank Pakorn Wongwaitayakornkul for his proof of concept work on a benchtop setup and preliminary design work. Additional thanks are given to the other Bellan group members for their technical assistance. This material is based upon work supported by the U.S. Department of Energy Office of Science, Office of Fusion Energy Sciences under Award Nos. DE-FG02-04ER54755 and DE-SC0010471, by the National Science Foundation under Award No. 1059519, and by the Air Force Office of Scientific Research under Award No. FA9550-11-1-0184.

[1]E. E. Fenimore and T. M. Cannon, Appl. Opt. **17**, 337 (1978).
[2]R. H. Dicke, Astrophys. J., Lett. **153**, L101 (1968).
[3]L. Mertz and N. Young, SPIE Milestone Series **128**, 44 (1996).
[4]R. Accorsi, Ph.D. thesis, MIT, 2001.
[5]A. Talebitaher, S. Springham, P. Shutler, P. Lee, and R. Rawat, J. Fusion Energy **31**, 234 (2012).
[6]M. E. Gehm, S. T. McCain, N. P. Pitsianis, D. J. Brady, P. Potuluri, and M. E. Sullivan, Appl. Opt. **45**, 2965 (2006).
[7]A. Haboub, A. A. MacDowell, S. Marchesini, and D. Y. Parkinson, Rev. Sci. Instrum. **85**, 063704 (2014).
[8]L. D. Baumert, *Digital Communications with Space Applications: Appendix 2* (Prentice-Hall, Inc., Englewood Cliffs, NJ, 1964).
[9]E. D. Nelson and M. L. Fredman, J. Opt. Soc. Am. **60**, 1664 (1970).
[10]R. Accorsi, F. Gasparini, and R. C. Lanza, Nucl. Instrum. Methods Phys. Res., Sect. A **474**, 273 (2001).
[11]S. C. Hsu and P. M. Bellan, Mon. Not. R. Astron. Soc. **334**, 257 (2002); e-print arXiv:astro-ph/0202380.
[12]D. Kumar and P. M. Bellan, Phys. Rev. Lett. **103**, 105003 (2009).
[13]OSI Systems, Inc., A2V-16 photodiode array, http://www.osioptoelectronics.com/standard-products/silicon-photodiodes/photodiode-arrays/multi-element-photodiode-array.aspx (2015).
[14]Y.-W. Chen and K. Kishimoto, Rev. Sci. Instrum. **74**, 2232 (2003).
[15]A. L. Moser, Ph.D. thesis, California Institute of Technology, 2012.
[16]A. L. Moser and P. M. Bellan, Nature **482**, 379 (2012).
[17]E. Caroli, J. B. Stephen, G. Di Cocco, L. Natalucci, and A. Spizzichino, Space Sci. Rev. **45**, 349 (1987).
[18]S. Miyamoto, Space Sci. Instrum. **3**, 473 (1977).
[19]S. C. Hsu and P. M. Bellan, Phys. Rev. Lett. **90**, 215002 (2003).
[20]S. C. Hsu and P. M. Bellan, Phys. Plasmas **12**, 032103 (2005); e-print arXiv:physics/0411089.
[21]J. J. M. in 't Zand, J. Heise, and R. Jager, Astron. Astrophys. **288**, 665 (1994).
[22]A. B. Giles, Appl. Opt. **20**, 3068 (1981).
[23]R. Accorsi and R. C. Lanza, Appl. Opt. **40**, 4697 (2001).